General Electromagnetic Simulation of Radar Signals Backscattered from Metallic Wind Turbines

Victoria Sgardoni* and Nikolaos Uzunoglu

Abstract—The backscattering of electromagnetic waves incident on a rotating metallic wind turbine (WT) is analyzed by using the Physical Optics method. The model developed is general and allows the computation of the spectral Doppler shift of the backscattered waves. All the parameters involved are taken into account, relative to incident wave direction, wind horizontal direction, WT geometric and electromagnetic properties. Numerical computations are carried out for various cases and presented relative to a search radar.

1. INTRODUCTION

The introduction of electrical energy generation technology by wind turbines (WTs) has demonstrated severe detrimental effects on ground detection radars of flying targets and, particularly, on airspace surveillance radars. These radars, making use of the Doppler phenomenon, are naturally affected by scattering from the wind turbines blades. The fact that radars based on Moving Target Indicator (MTI) or Moving Target Detection (MTD) technologies operate on the principle of rejecting stationary targets — mainly the scattering from the earth surface with zero or near-zero Doppler frequency shift — while taking advantage of the Doppler frequency shift from moving or flying vehicles (airplanes) in order to detect and track targets results in these radars being severely affected by a rotating object such as the WT blades.

The fact that each rotating blade of length L and angular rotational speed Ω rad/sec develops a linear speed ranging from $v_{\min} = 0$ (at the rotation axis "root") to $v_{\max} = \Omega L$ (at the blade tip) will create a continuous signal "curtain" with Doppler shift f_d, depending on the radiation incidence angle. If the propagation direction of an incident wave to the WT lies on the same plane of the blades' rotation (usually there are three turbine blades at an angle of $120°$ from each other), the full range of Doppler frequencies will occur:

$$-f_{d,\max} < f_d < f_{d,\max} \tag{1}$$

where $f_{d,\max} = 2v_{\max}f_0/c$, $c = 3 \cdot 10^8$ m/sec is the speed of EM radiation in vacuum, and f_0 is the carrier frequency of the radar signal, being usually in the microwaves zone (1–40 GHz).

The other extreme case is when the blades rotation plane is perpendicular to the incident radiation, in which case it can be deduced easily, theoretically, that the Doppler frequency shift will be zeroed.

It was quickly ascertained that this phenomenon has severe effects not only on the radars used by the defense forces of a country, but on the civil aviation radars as well, since they use similar types of radars that are based on the same physical principles.

Initially, the relevant Departments in charge from the Ministries of Defense set out a strict set of rules for the installation of WTs, attempting to place them in the "shadows" of radars. However,

later it transpired that it was impossible to implement this policy, because the maximization of electric energy production from wind potential requires the installation of WTs on mountains and, indeed, on the boundary lines of mountain ranges. Under these circumstances new principles were adopted for "milder" radar disruption. For example, a radar signal ray should not be completely interrupted by the WT "rotation disk", in the worst case. Also, the WTs distance from a radar should be greater than a minimum limit, so that scattering from the WT stable parts does not cause signal saturation at the input stages of the radar receivers.

This issue has been the subject of research papers from a number of authors since 2005. Nevertheless, taking into account the importance of the matter in national defense issues, as well as civil aviation security issues, there is not enough bibliography and publications on the subject. In a report by RTO NATO titled *The Effects of Wind Farms on NATO Radar Systems (SET 128/RTG-07) (23/8/2016)*, a program of inter-state collaboration was proposed in order to study the phenomenon. In the last 5 years a number of publications were presented in international conferences (mostly) that address the issue from a measurements' perspective mainly [1–5].

The USA Congress has been concerned about this issue, at a political level, as early as 2006 [6]. Several researchers have addressed the issue studying the radar cross section of WTs, attempting to reduce the effects of WTs on radars [7]. Some proposals have been made to use methods based on signal processing in radars, in order to encounter the phenomenon described to a lesser extent [8–10].

To the best of our knowledge the scattering phenomenon of incident waves has not been analyzed by electromagnetic analysis so far, and it is not possible to make a quantitative comparison with results from other methods. In this article an electromagnetic analysis based on Physical Optics (P.O.) method is presented, and numerical results are reported for various indicative cases.

2. ELECTROMAGNETIC ANALYSIS OF THE BACKSCATTERING OF WAVES BY WIND TURBINE ROTATING BLADES

The characteristic WT structure is shown in Fig. 1. The structure consists of the rotating 3-metallic blades and a vertical tower supporting the axis of the blades. The following analysis is focused only on the rotating part of WT, as only this will generate reflected signals with a Doppler frequency shift.

Figure 1. General geometry of a wind turbine (courtesy of Hellenic Wind Energy Association).

Given that the radiation from a radar has a wavelength ranging from tens of centimeters up to a few centimeters (1–20 GHz), while the blades are tens of meters in length and tens of centimeters in diameter, in the electromagnetics problem addressed, the dimensions of the scatterer are much larger than the wavelength. Therefore, in such a case it is appropriate to use high frequency methods, as, practically, it is very difficult to apply numerical analysis methods. In this work the Physical Optics (P.O.) method is used.

The P.O. method is based on the following principles:

a) It is assumed that the electromagnetic waves are scattered only on the surfaces where the radiation rays are directly incident considering them as geometric rays. Thus, the edge diffraction phenomena are ignored.

b) On the surfaces that are directly illuminated, the current induced by the incident EM wave, $\mathbf{J_s}$ (A/m), is computed by the equation:

$$\mathbf{J_s} = 2\hat{\mathbf{n}} \times \hat{\mathbf{H}}_{\mathbf{inc}} \tag{2}$$

where $\hat{\mathbf{n}}$ is a unit vector perpendicular to the surface, towards the outer side, and $\hat{\mathbf{H}}_{\mathbf{inc}}$ is the magnetic component of the incident magnetic field, which is known and defined as:

$$\hat{\mathbf{H}}_{\mathbf{inc}} = \hat{\mathbf{h}}C_0 e^{(-jk_o R_o)} e^{\left(-jk_o \hat{k}_\mathbf{i} \cdot \hat{r}\right)} \tag{3}$$

where

$$C_0 = \frac{\sqrt{\dfrac{P_t G_t}{60\pi}}}{(4\pi R_0)}$$

$P_t G_t$ is the effective radiated power from the radar antenna beam, with G_t the gain of the radar antenna in the direction of the WT and P_t the transmitted power of the radar; $\hat{\mathbf{h}}$ is the unit vector of the magnetic field that is perpendicular to the incidence direction and the associated electric field; R_0 is the distance of the radar antenna center O' from the reference point O on the WT rotation axis, defined as the coordinates' origin for the WT, as shown in Fig. 2; $\hat{k}_\mathbf{i}$ is the unit vector defining the direction of incidence of the EM wave from the radar to the WT; $\hat{r}$ is the position vector of a random point on the turbine blade, and $k_o = \omega/c$ is the propagation constant (wavenumber) in free space; ω is the angular frequency of the electromagnetic radiation.[†]
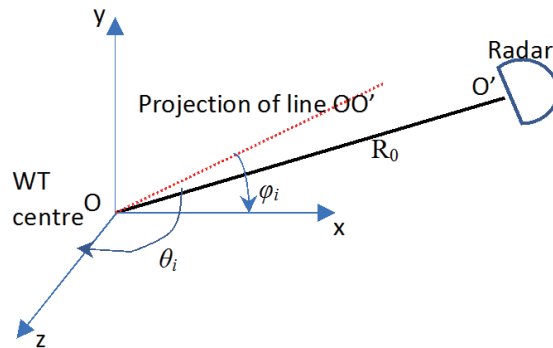

Figure 2. Definition of distance between WT and radar, R_0, and of the angles θ_i, φ_i.

Knowing the value of $\mathbf{H_0}$ the surface current can be computed on the surface current $\mathbf{J_s}$ (A/m) on the blade surface that is illuminated directly from the incident wave.

c) For the schematic modelling of each blade, it is assumed that a blade consists of coaxial cylinders of finite length, where each part has a radius as shown in Fig. 3(a). Scattering is affected by the curvature radius. The choice of cylindrical geometry to model the blade is justifiable, since the local

---

[†] The angular frequency must be considered as the spectral variable that would be used for Fourier analysis.

radar cross section at each point on the blade is determined principally by the curvature radius, and therefore selecting an equal radius cylinder is expected to be a good approximation. In this work, it is assumed that the radii of the finite cylinders are equal for the calculations. Nevertheless, the method proposed can be generalized easily.

3. FORMULATION OF THE ELECTROMAGNETICS PROBLEM

The geometry of a WT is defined in Figs. 2 and 3(b), taking into account the descriptions of the previous sections. Axis y is local vertical and remains unchanged. When the wind direction changes, the rotation axis of the blades, z, will change direction in the horizontal plane, as well as the axis x.

(a)   (b)
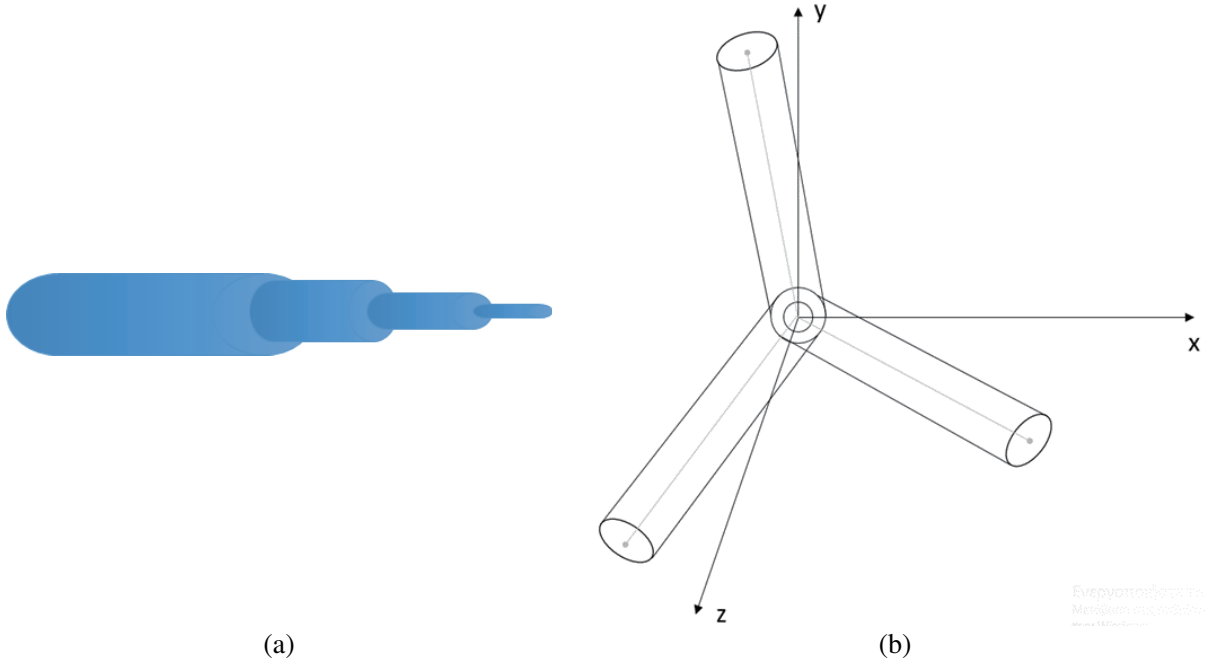
Figure 3. (a) Schematic model of a blade, (b) Geometry of a wind turbine with 3 blades at 120° to each other.

The incident wave properties with respect to the direction of the incident wave $\hat{\mathbf{k}}_\mathbf{i}$ (locally as a plane wave) and the magnetic field polarization vector are both defined in the same rotating coordinates system.

Following the above hypotheses, it is assumed that a radar radiates EM energy on a WT. The electric and magnetic fields, effective values, which are incident on the WT from the radar, are defined by the following equations:

$$\mathbf{E_{inc}} = \hat{\mathbf{e}}\frac{\sqrt{2P_tG_tZ_o}}{4\pi R_o}e^{(-jk_oR_o)}e^{\left(-jk_o\hat{k}_\mathbf{i}\cdot\hat{r}\right)} \tag{2a}$$

$$\mathbf{H_{inc}} = \hat{\mathbf{h}}\frac{\sqrt{2P_tG_t}}{4\pi R_o\sqrt{Z_o}}e^{(-jk_oR_o)}e^{\left(-jk_o\hat{k}_\mathbf{i}\cdot\hat{r}\right)} \tag{2b}$$

where $Z_0 = 120\pi\,(\Omega)$ is the wave resistance of free space.

In this work, the time dependency term, expressed as $\exp(j\omega t)$, is not shown in the whole analysis. The terms P_tG_t, R_o, k_o were defined for Eq. (1b).

The remaining terms are:

$\hat{k}_\mathbf{i}$ is the incidence radiation unit vector, which is defined as

$$\hat{\mathbf{k}}_\mathbf{i} = -\hat{\mathbf{x}}\sin\theta_i\cos\varphi_i - \hat{\mathbf{y}}\sin\theta_i\sin\varphi_i - \hat{\mathbf{z}}\cos\theta_i \tag{3}$$

and θ_i, φ_i are the angles in the Cartesian system of Fig. 2 related to the spherical coordinates. θ_i is defined as the angle between line OO' and the z axis. φ_i is the angle between the projection of line OO' on the xOy plane and x axis. $\hat{\mathbf{x}}$, $\hat{\mathbf{y}}$, $\hat{\mathbf{z}}$ are the unitary vectors of the cartesian system of Fig. 3(b).

The unitary vectors $\hat{\mathbf{e}}$, $\hat{\mathbf{h}}$ are the polarization vectors of the E and H fields, respectively. Especially for vertical polarisation of the electric field, the electrical polarization vector is defined as:

$$\hat{\mathbf{e}}_{\mathbf{v}} = -\hat{\mathbf{x}} \cos \theta_i \cos \varphi_i - \hat{\mathbf{y}} \cos \theta_i \sin \varphi_i + \hat{\mathbf{z}} \sin \theta_i \tag{4}$$

while for horizontal polarization of the electric field:

$$\hat{\mathbf{e}_{\mathbf{h}}} = -\hat{\mathbf{x}} \sin \varphi_i + \hat{\mathbf{y}} \cos \varphi_i \tag{5}$$

A random point on the surface is described by the position vector $\mathbf{r}$:

$$\mathbf{r} = (\hat{\mathbf{x}} \cos (\Theta (t)) + \hat{\mathbf{y}} \sin (\Theta (t))) \zeta + \alpha \hat{\mathbf{n}} \tag{6}$$

where $\hat{\mathbf{n}}$ is the unitary vector vertical to the surface of the cylindrical blade, ζ the distance of $\mathbf{r}$ from point O along the blade, and α the blade radius, as shown in Fig. 4. $\Theta(t)$ is the rotation angle of the blade around the z axis, defined as $\Theta(t) = \Omega t$, where Ω is the angular rotational speed of the blades, and t is time.
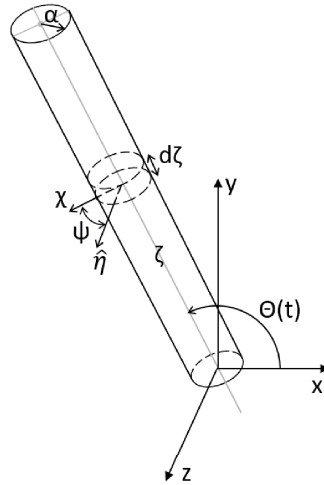

Figure 4. Geometry of a WT blade.

In carrying out the calculations the prime interested in the unitary polarization vector of the magnetic field $\hat{\mathbf{h}}$. Since for air surveillance and detection radars, horizontal electric polarization is usually used, the vector of the magnetic field $\hat{\mathbf{h}} = \hat{e}_{\mathbf{v}}$ will lie in the vertical plane; it is defined as follows.

Vector $\hat{\mathbf{n}}$ is the unitary vector vertical to the cylindrical blade and is given by the following formula, when the angle ψ is defined for a cross-section of the cylindrical blade.

$$\hat{\mathbf{n}} = (\hat{\mathbf{x}} \sin (\Theta (t)) - \hat{\mathbf{y}} \cos (\Theta (t))) \cos \psi + \hat{\mathbf{z}} \sin \psi \tag{7}$$

$\Theta(t)$ is the rotation angle of the blade around the z axis, defined as $\Theta(t) = \Omega t$ as above.

According to the above:

$$\hat{\mathbf{h}_{\mathbf{v}}} = -\hat{\mathbf{x}} \cos \theta_i \cos \varphi_i - \hat{\mathbf{y}} \cos \theta_i \sin \varphi_i + \hat{\mathbf{z}} \sin \theta_i \tag{8}$$

and

$$\hat{\mathbf{h}_{\mathbf{h}}} \cdot \hat{\mathbf{k}_{\mathbf{i}}} = 0$$
$$\hat{\mathbf{k}_{\mathbf{i}}} = \hat{\mathbf{e}}_{\mathbf{v}} \times \hat{\mathbf{h}_{\mathbf{v}}} = \hat{\mathbf{e}}_{\mathbf{h}} \times \hat{\mathbf{h}_{\mathbf{h}}} \tag{9}$$

where $\times$ denotes the cross product of vectors, and $\hat{\mathbf{k}_{\mathbf{i}}}$ is defined in Eq. (3).

4. CALCULATION OF THE DOPPLER FREQUENCY SHIFT

Given that the blades are solid and rotate around the z axis, all points of the cylindrical blade move for the same distance ζ with the same linear velocity $\mathbf{v}$, defined by the formula:

$$\mathbf{v} = \frac{d\mathbf{r}}{dt} = \zeta\Omega\left(-\sin\Theta\left(t\right)\hat{\mathbf{x}} + \cos\Theta\left(t\right)\hat{\mathbf{y}}\right) \tag{10}$$

because the term $\alpha\hat{\mathbf{n}}$ in Eq. (6) does not change in time.

According to the well-known formula for the Doppler frequency shift f_d:

$$f_d = -\frac{2\mathbf{v}.\mathbf{k_i}}{c}f_0 \tag{11}$$

where $f_0 = \frac{\omega_0}{2\pi}$ is the radar carrier (central) radiation frequency, in Hz.

Substituting Eqs. (3), (10), and (11), the following Doppler shift relation is obtained:

$$f_d = 2\Omega\zeta\frac{f_0}{c}\left(\sin\theta_i\sin\left(\varphi_i - \Theta\left(t\right)\right)\right) \tag{12}$$

which takes its maximum value for $\zeta = L$, $\theta_i = 90°$, as $|f_{D,MAX}| = 2\Omega L\frac{f_0}{c}$.

5. PHYSICAL OPTICS

Realizing that the Doppler shift increases linearly with distance ζ, the scattering by a small strip of the blade $(\zeta, \zeta + d\zeta)$ is computed. The length $d\zeta$ is determined by the spectral resolution of the Doppler filters. It should be noted that the P.O. method is independent from the polarization of the incident wave.

In order to implement the P.O. method, it is necessary find the angle ψ^* at which the radiation strikes meridionally the surface of the cylindrical blade. This is achieved by calculating the inner product $\hat{\mathbf{n}}\cdot\hat{\mathbf{k_i}}$ and finding the angle ψ at which the product gets its maximum value.

$$\hat{\mathbf{n}}\cdot\hat{\mathbf{k_i}} = -\sin\Theta\left(t\right)\cos\psi\sin\theta_i\cos\varphi_i + \cos\Theta\left(t\right)\cos\psi\sin\theta_i\sin\varphi_i - \cos\theta_i\sin\psi$$

By computing the derivative of the above relation with respect to ψ and finding the value of $\psi = \psi^*$ for which the derivative is zero, it is found that:

$$\sin\Theta(t)\sin\psi\sin\theta_i\cos\varphi_i - \cos\Theta(t)\sin\psi\sin\theta_i\sin\varphi_i - \cos\theta_i\cos\psi = 0 \Longrightarrow$$

$$\tan\psi^* = \frac{{}^1\!/\tan\theta_i}{\sin\Theta(t)\cos\varphi_i - \cos\Theta(t)\sin\varphi_i} = \frac{1}{\tan\theta_i}\frac{1}{\sin\left(\Theta\left(t\right) - \varphi_i\right)} \tag{13}$$

In computing the ψ^* angle by Eq. (13) always the $\hat{\mathbf{n}}\cdot\hat{\mathbf{k_i}} < 0$ is selected considering the two valued $\arctan(\psi)$ function. This is because the incident wave propagation vector should in opposite direction with the unit vector on the cylindrical surface at the meridionally line.

On the partition of the blade surface $(\zeta, \zeta + d\zeta)$ along the axis and at angle $\alpha d\psi$, a flow of electric current is developed on the surface:

$$\mathbf{J}_s\left(\psi, \zeta\right) = 2\hat{\mathbf{n}} \times \mathbf{H_{inc}} \tag{14}$$

where $\mathbf{H_{inc}}$ is the magnetic field defined in Eq. (2b). Considering that an elementary current from a surface islet $(d\zeta, \alpha d\psi)$ generates an electrical field at a distance from it, it is found that:

$$\mathbf{dE_s} = -j\omega\mu_0(1 - \hat{\mathbf{k_s}}\hat{\mathbf{k_s}}))\cdot\mathbf{J}_s\left(\psi, \zeta\right)\frac{e^{(-jk_0R_0)}}{4\pi R_0}e^{\left(jk_0\hat{k_s}\cdot\mathbf{r}\right)}d\zeta\alpha d\psi \tag{15}$$

where $\hat{\mathbf{k_s}}$ is the unit vector parallel to scattering direction and $\mu_0 = 4\pi10^{-7}$ (H/m) the free space magnetic permeability.

The term $(\mathbf{1} - \hat{\mathbf{k_s}}\hat{\mathbf{k_s}})$ refers to the "transversal dyadic" since $\mathbf{1}$ is the unitary dyadic $(\mathbf{1}\cdot\mathbf{A} = \mathbf{A})$, and the term $\hat{\mathbf{k_s}}\hat{\mathbf{k_s}}$ refers to the lengthways component. The unitary vector $\hat{\mathbf{k_s}} = -\hat{\mathbf{k_i}}$ is in the direction of backscattering, which, in our case, is in the opposite direction to the incident wave, since a monostatic radar is assumed (with a common antenna for emission and reception).

Combining Eqs. (14) and (15):

$$\mathbf{dE_s} = -j\omega\mu_o \left(\mathrm{I} - \hat{\mathbf{k}}_\mathbf{s}\hat{\mathbf{k}}_\mathbf{s}\right) \cdot \mathbf{J}_s\left(\psi,\zeta\right) e^{\left(-j\hat{k}_\mathbf{i}\cdot\{(\hat{x}\cos\Theta(t)+\hat{y}\sin\Theta(t))\zeta+\hat{n}a\}\right)} e^{(j2\pi f_d t)} \frac{e^{(-jk_o R_o)}}{4\pi R_o} a d\psi d\zeta$$

and after integration on the blade strip $(\zeta, \zeta + d\zeta)$, from $\psi = \psi^* - \pi/2$ to $\psi = \psi^* + \pi/2$ (assuming that a finite half cylinder receives radiation), the following relation is derived:

$$\mathbf{\Delta E_{s,f_d}} = -j\omega\mu_o \int\limits_{\zeta}^{\zeta+\Delta\zeta} d\zeta \int_{\psi^*-\frac{\pi}{2}}^{\psi^*+\frac{\pi}{2}} \alpha d\psi \left(\mathbf{1} - \hat{\mathbf{k}}_\mathbf{i}\hat{\mathbf{k}}_\mathbf{i}\right) \cdot \left(\hat{\mathbf{n}}\left(\psi\right) \times \hat{\mathbf{h}}_\mathbf{h}\right) \cdot \frac{2\sqrt{2P_t G_t}}{\left(4\pi R_o\right)^2 \sqrt{Z_o}}$$

$$e^{-2j\hat{k}_\mathbf{i}\cdot\{(\hat{x}\cos\Theta(t)+\hat{y}\sin\Theta(t))\zeta+\hat{n}A\}} e^{-2jk_o R_o} e^{j(\omega+f_d)t} \tag{16}$$

where the factor $e^{j(\omega+f_d)t}$ reintroduces the time dependency.

Assuming that the receiver has Doppler resolution Δf_d it is found that:

$$\Delta f_d = 2\Omega d\zeta \frac{f_0}{c} \sin\theta_i \sin\left(\varphi_i - \Theta(t)\right) \tag{17}$$

After resolving the integral with respect to ζ, it is derived that:

$$\mathbf{\Delta E_{f_d}} = C_o\left(\Theta(t)\right) e^{2jk_o\zeta} \frac{\sin(k_o\Delta\zeta\sin\theta_i\cos(\varphi_i - \Theta(t))}{\sin\theta_i\cos(\varphi_i - \Theta(t))} \mathbf{\Lambda}\left(\Theta(t), \theta_i, \varphi_i\right) \cdot \hat{\mathbf{e}}_\mathbf{h} \tag{18}$$

where

$$C_o = -2j\omega\mu_o \left(\hat{\mathbf{I}} - \hat{\mathbf{k}}_\mathbf{s}\hat{\mathbf{k}}_\mathbf{s}\right) \frac{\sqrt{2P_t G_t}}{\left(4\pi R_o\right)^2 \sqrt{120\pi}} a e^{j(\omega+f_d)t}$$

C_o is a function of $\Theta(t)$ because of f_d, and $\hat{\mathbf{e}}_\mathbf{h}$ is the horizontal polarization vector.

From Eq. (18) it is observed that when $\cos(\varphi_\iota - \Theta(t)) = 0$, the reflection is maximum, i.e., $\varphi_\iota - \Theta(t) = \pm\pi/2$.

The vector function Λ is defined as:

$$\mathbf{\Lambda}\left(\Theta(t), \theta_i, \varphi_i\right) = \int_{\psi^*-\frac{\pi}{2}}^{\psi^*+\frac{\pi}{2}} d\psi\{\hat{\mathbf{x}}\sin\psi\left(\cos\theta_i\sin\varphi_i - \cos\Theta(t)\sin\theta_i\right) - \hat{\mathbf{y}}\left(\cos\psi\sin\Theta(t)\sin\theta_i\right.$$

$$\left. + \cos\theta_i\cos\varphi_i\sin\psi\right) - \hat{\mathbf{z}}(\cos\theta_i\sin\varphi_i\sin\Theta(t)\cos\psi - \cos\Theta(t)\sin\psi\cos\theta_i\cos\varphi_i)\}$$

$$e^{2k_o aj(\sin\Theta(t)\cos\psi\sin\theta_i\cos\varphi_i+\cos\Theta(t)\cos\psi\sin\theta_i\sin\varphi_i-\cos\theta_i\sin\psi)} \tag{19}$$

The term $\mathbf{\Lambda}$ will be evaluated numerically as a complex vector along the three components x, y, z, for each value of $\Theta(t)$, θ_i, and φ_i. The values of θ_i and φ_i are determined by the incidence angle of the radar EM wave on the WT blade.

Equation (18) for $\Delta\boldsymbol{E}_\mathbf{fd}$ has the form of a sinc$(\cdot)$ function that is maximized for maximum reflection, when

$$\cos\left(\varphi_i - \Theta(t)\right) = 0 \Longrightarrow \varphi_i - \Theta(t) = \pm\frac{\pi}{2}$$

Given that there are three blades with instantaneous positions determined by $\Theta(t)$, $\Theta(t) + 120°$, $\Theta(t) - 120°$, the signals reflected to the radar from the WT must be calculated independently at any given time t.

It should be noted that shadowing between the blades is ignored, as it is a secondary minor phenomenon.

Calculations are performed for each blade independently, but in the end the results are presented in terms of two independent variables in the time domain, relative to the blades rotation angle and the Doppler shift. The addition of the waves scattered by the corresponding blades can be performed for the same time instant and the same Doppler shift (as the central frequency of the relevant Doppler filter):

$$\mathbf{\Delta E_{f_d,TOTAL}} = \mathbf{\Delta E_{f_d}}\left(\Theta(t)\right) + \mathbf{\Delta E_{f_d}}\left(\Theta(t) + 120°\right) + \mathbf{\Delta E_{f_d}}\left(\Theta(t) - 120°\right) \tag{20}$$

The present computational method calculates the radar cross-section (RCS) of the WT corresponding to the specific Doppler bin Δf_d, which is relative to the spectral resolution of the radar receiver. The related RCS is computed easily by the equation

$$\sigma(\Delta f_d) = 4\pi R_o^2 |\Delta \mathbf{E_{fd,TOTAL}}|^2 / |\mathbf{E_{inc}}|^2$$

when R_o goes to infinity. In the case of a real target with a near Doppler frequency shift, having an RCS of value σ_o, the ratio $\sigma(\Delta_{fd})/\sigma_o$ determines the detectability of the target when it is close to the WT and inside the same delay time bin.

6. NUMERICAL CALCULATIONS AND SIMULATIONS

Implementing the analysis of Sections 2 to 5, a simulation software program calculating the electric field E has been developed, due to radar radiation scattered by the rotating blades of a WT. The WT model used is based on a WT with 3 blades at 120° angles between them, as shown in Fig. 5. The simulation software was written in MATLAB[‡].
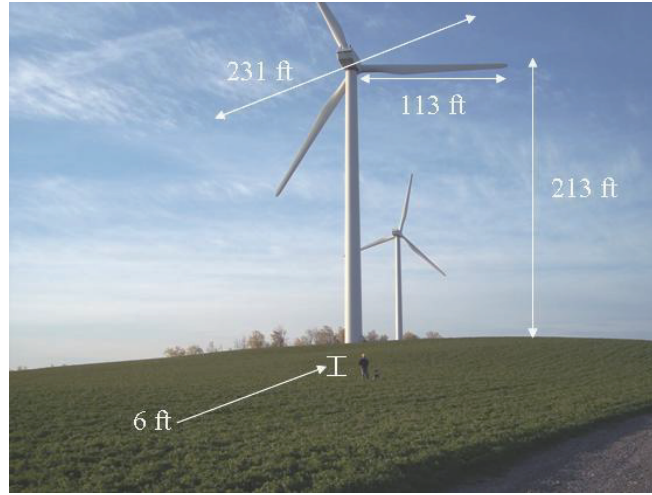

Figure 5. Wind turbine dimensions [11].

The simulator computer program calculates the electric field component along the incident polarization ΔE due to scattering at each surface islet $(d\zeta, \alpha d\psi)$ of each blade. After the integration of ΔE with respect to $d\zeta$, the electric field generated on each blade is evaluated according to Eqs. (18) and (19). The calculation of the frequency Doppler shift is based on Eq. (12).

Realistic parameters have been used for the modelling of a WT and the radiation from an MTI radar. Specifically, a WT with blade length $L = 34$ m (≈ 113 ft) is taken, representative of numerous WTs [11]. Two values were considered for the angular rotational speed Ω rad/sec when there is wind, a) 7 rpm corresponding to $\Omega = 0.23\pi$ rad/sec, a low rotation speed for low intensity wind, and b) 19 rpm corresponding to $\Omega = 0.633\pi$ rad/sec, a very high rotation speed for high-speed winds (considering that the wind speed varies between 0 and tens of km/h in extreme conditions). The angular speed is expected in the range 9–19 rpm [12], for modern WTs of 2 MW power.

The blade radius is assumed $\alpha = 0.5$ m, on average, as the radius is considered constant along the whole length of the blade, in order to simplify the modelling, although in reality blades are thinner at the tip and larger near the root, as shown in Fig. 6 [12]. In general, the blade diameter is less than 2.5 m.

Regarding the radar parameters to evaluate the radiation from an MTI/MTD radar, it is assumed the radar transmitted power $P_t = 10^4$ W, the antenna gain $G_t = 33$ dBi, and the carrier frequency

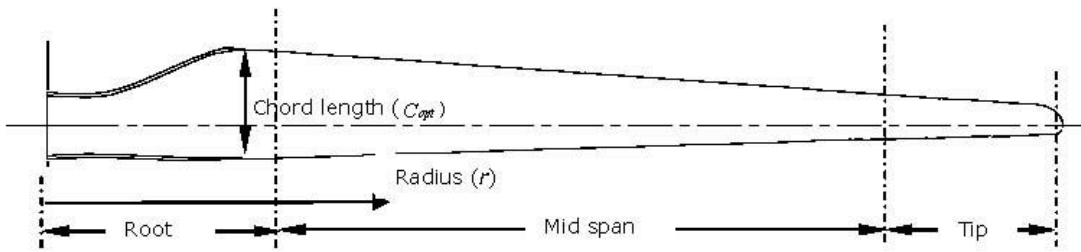[‡] https://www.mathworks.com/academia/tah-portal/ntua-31572547.html

Figure 6. Design of a modern WT blade [12].

$f_0 = 2.7\,\text{GHz}$. It is assumed that the radar is located at a distance $R_0 = 20\,\text{km}$ from the WT (distance considered between the WT rotation centre and the radar antenna centre).

The electric field strength on each blade, ΔE, is evaluated from each surface islet $d\zeta$ of the blade, with step $d\zeta = 0.33\,\text{m}$, every $\Delta t = 0.01\,\text{sec}$, for a full rotation of the blade. It is evaluated as a function of Doppler frequency shift, due to the angular rotational speed Ω according to Eqs. (17), (18), (19), assuming that the Doppler frequency resolution is $\Delta f_d = 5\,\text{Hz}$ at the radar receiver. After evaluating the electric field strength ΔE along each blade (as a vector) at the position it has, at each time t, the total electric field, E_{TOT}, is computed according to Eq. (20).

The simulation for the evaluation of the electric field and the Doppler frequency shifts during a complete rotation was performed assuming horizontal polarization (based on the polarization vectors in Eqs. (4) and (5)), for different values of the angles θ_i and φ_i.

Simulation results for the electric field of each blade, ΔE, and the total electric field by taking into account the contribution of three blades (rotating with $120°$ angular spatial difference), E_{TOT}, are presented in the following sections, for different sets of angles θ_i and φ_i, as noted in each section. In the following subsections A, B, C, the corresponding results are given in Figs. 7–10 which are obtained for angular rotation speed $\Omega = 0.23\pi\,\text{rad/sec}$, i.e., $7\,\text{rpm}$. In section D and Figs. 11 to 13, results are given for angular rotation speed $\Omega = 0.633\pi\,\text{rad/sec}$, i.e., $19\,\text{rpm}$. Section E presents the results for the evaluation of the total electric field, E_{TOT}.

A) Assuming that the rotation plane of the blades is perpendicular to the ground, the following graphs show the magnitude of the electric field, ΔE, generated on each of the three blades for angles $\theta_i = 89°$, and $\varphi_i = 0$, $10°$, and $45°$.

The magnitude of the electric field ΔE is calculated as a function of the rotation angle $\Theta(t)$ at time t, and the Doppler shift f_d produced at that time t, at each point of the blade (at distance ζ from its root). Thus, the electric field magnitude, ΔE, is shown as a 3D plot, where the independent axes are the rotation angle $\Theta(t)$ and Doppler shift f_d.

From the graphs in Figs. 7 and 8, showing the electric field magnitude ΔE on each blade with respect to Doppler shift f_d and the rotation position in time $\Theta(t)$, the following observations can be done:

- The electric field magnitude ΔE is symmetrical with respect to $\Theta(t)$ and Doppler frequency f_d in all cases.
- The graphs of ΔE for each of the three blades, at angles $\Theta(t)$, $\Theta(t) + 120°$, $\Theta(t) - 120°$ respectively, have the same form but with a phase difference corresponding to the rotation angle difference $\Theta(t)$.
- The electric field magnitude ΔE is periodic and resembles the shape of a sine wave (on the plane of axis $\Theta(t)$ and f_d). This is expected due to the blades' rotation at a constant speed.
- The range of values that ΔE takes differs according to the angles θ_i and φ_i considered. In Figs. 7, 8, it is assumed that $\theta_i = 89°$ and $\varphi_i = 0$, $10°$, $45°$.
- In the graph for each blade, the fluctuation of the electric field magnitude ΔE between minimum and maximum values is small (values in the order of 10^{-4}).
- In Fig. 8 the sidelobes of ΔE are attenuated for larger angles φ_i, as it increases from $0°$ and $10°$ to $45°$, while the central lobe is accentuated respectively (to 2×10^{-3}).
- The range of Doppler shifts f_d in the above graphs, for $\theta_i = 89°$, is similar, $[-442, 442]\,\text{Hz}$.

(a)

(b)

(c)

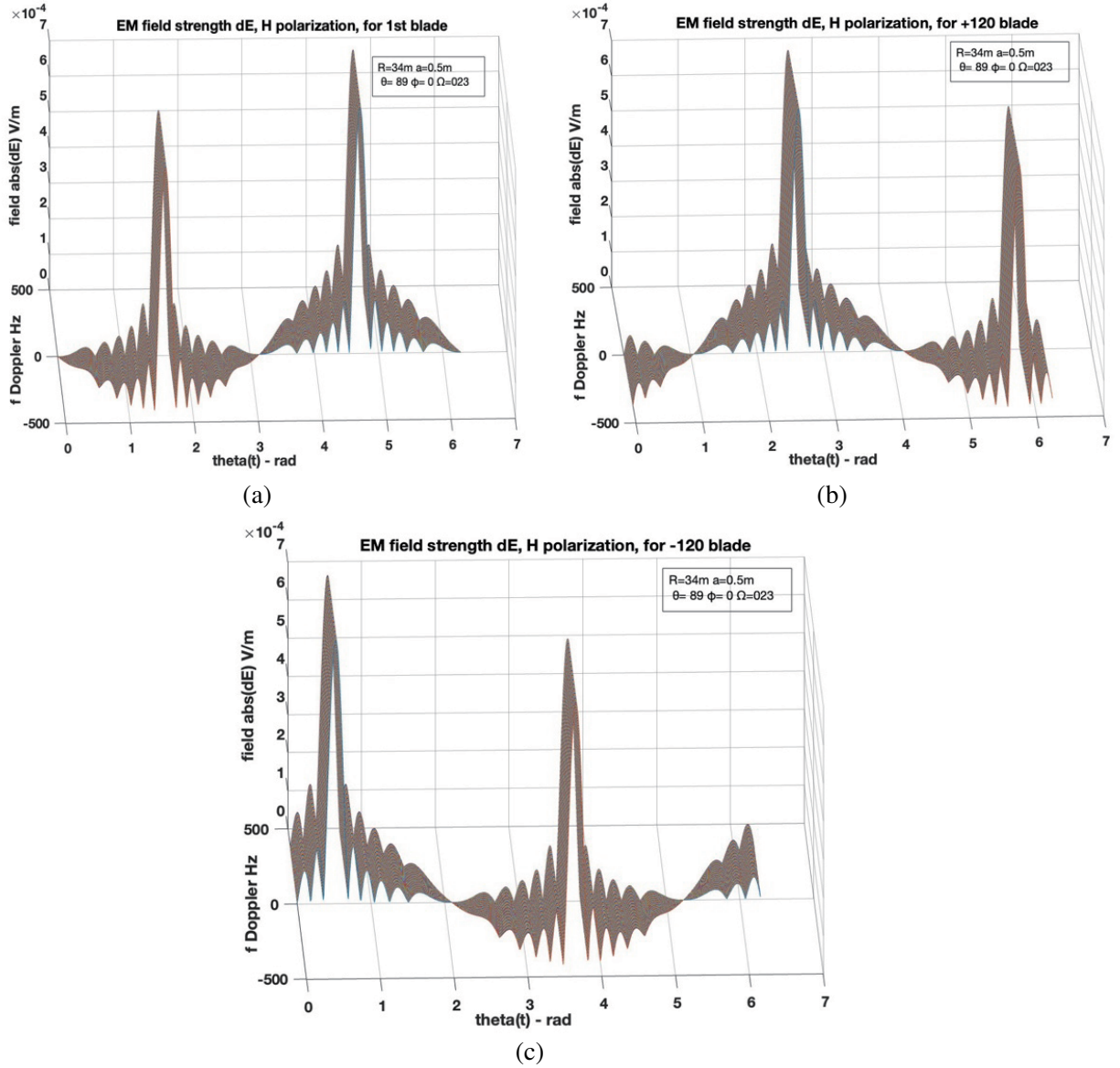**Figure 7.** (a), (b), (c) EM field strength $\Delta E(f_d, \Theta(t))$ on each blade, for $\theta_i = 89°$, $\varphi_i = 0°$, $\Omega = 0.23\pi$ rad/sec.

Figures 7 and 8 show clearly that the backscattered signals spread as a sinusoidal in time, $\Theta(t)$. Since the graph of the electric field ΔE on each blade has the same form but shifted by Θ, in the following sets of results only graphs of one blade will be shown.

B) Next, results are shown for the magnitude of the electric field ΔE generated on one blade for small angles θ_i, when $\theta_i = 20°$, and for $\varphi_i = 0°$, $10°$. The rotation plane of the blades is assumed perpendicular to the ground plane.

In the graphs of Fig. 9, for $\theta_i = 20°$ it can be observed that:

- When $\varphi_i = 0°$ the variation of ΔE during a full rotation is smoother than that for the bigger angle θ_i considered previously in Figs. 7 and 8. The field ΔE is of the same order of magnitude as when $\theta_i = 89°$, in Figs. 7 and 8.

- The periodicity of the electric field magnitude ΔE can be clearly observed.

- The range of Doppler shifts is smaller than that in Figs. 7, 8, in the range of $[-150, 150]$ Hz. This is obvious for small values of θ_i, from formula (12) for the calculation of Doppler shift.
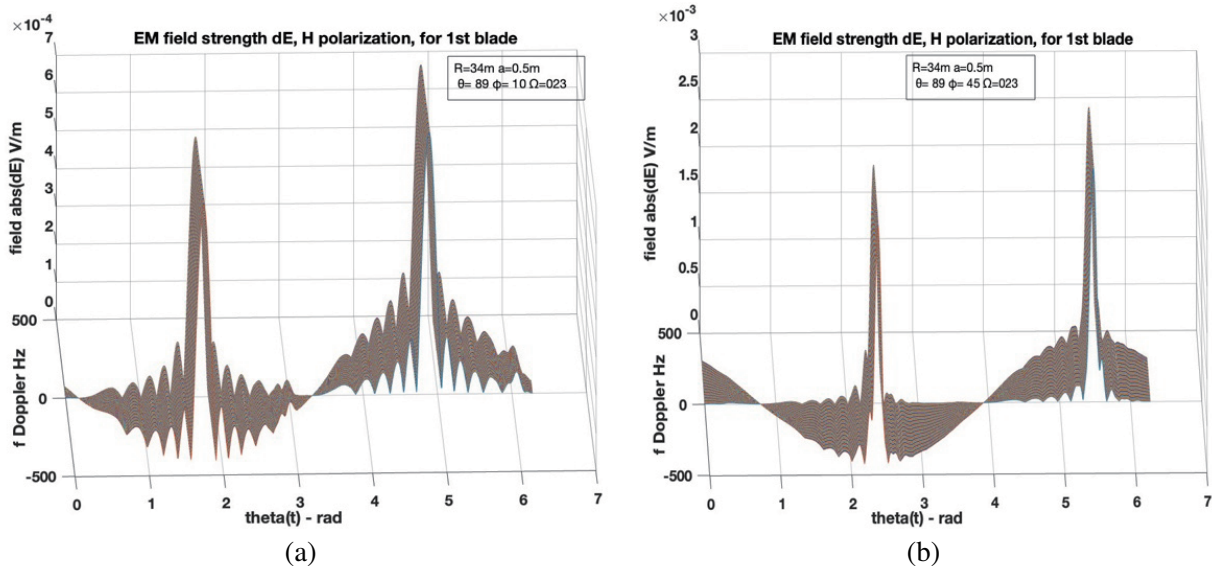
(a)

(b)

Figure 8. (a), (b) EM field strength $\Delta E(f_d, \Theta(t))$ on one blade, for $\theta_i = 89°$, $\varphi_i = 10°$, $45°$, $\Omega = 0.23\pi\,\mathrm{rad/s}$.
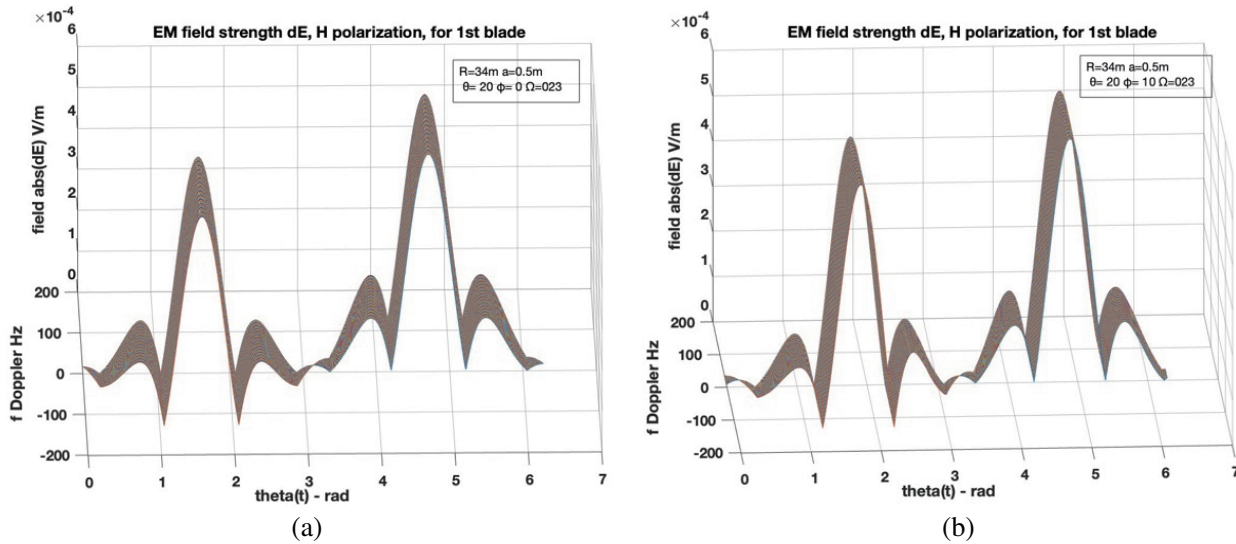

(a)

(b)

Figure 9. (a), (b) EM field strength $\Delta E(f_d, \Theta(t))$ on one blade, for $\theta_i = 20°$ and $\varphi_i = 0$, $10°$, $\Omega = 0.23\pi\,\mathrm{rad/sec}$.

C) Next, the case when angle $\theta_i = 0°$ and $3°$ is examined, i.e., values close to zero.
In the graphs of Fig. 10, it can be observed that:

- For $\theta_i = 0°$ (and $\varphi_i = 10°$) the electrical field is zero, which is justified from Eqs. (18) and (19). That is, when the blades rotation plane is perpendicular to the incident wave direction ($\mathbf{k_i}$) zero backscattering energy is observed.

- In Fig. 10(b) for $\theta_i = 3°$, the graph of the electrical field ΔE has very few variations in time (with respect to bigger angles θ_i), it is periodic and smooth, of similar magnitude as that for bigger angles θ_i (in the order of 10^{-4}).

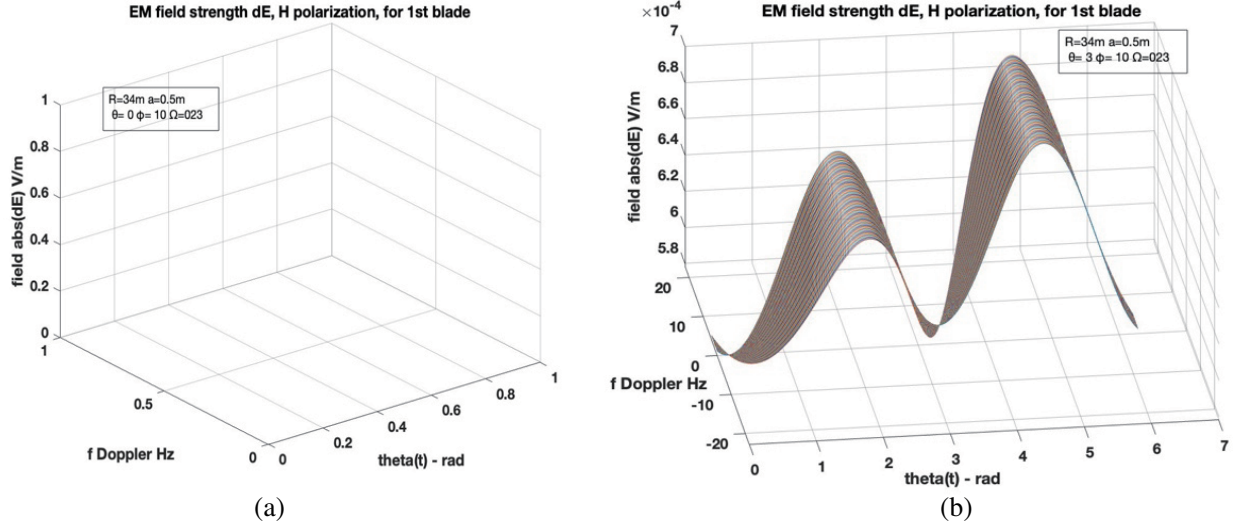- The range of Doppler shifts is even smaller than that in Fig. 9, with range $[-23, 23]\,\mathrm{Hz}$, so it is

Figure 10. (a), (b) EM field strength ΔE $(f_d, \Theta(t))$ on one blade, $\theta_i = 0°$ and $3°$, $\varphi_i = 10°$, $\Omega = 0.23\pi$ rad/sec.

obvious that the smaller the angle θ_i is, the smaller the Doppler shifts f_D are, reaching 0 when $\theta_i = 0$.

D) The following simulations were carried out for angular rotational speed $\Omega = 0.633\pi$ rad/sec, or 19 rpm, showing representative graphs for $\theta_i = 3°$, $20°$, $89°$ and $\varphi_i = 0$, $10°$.

In Figs. 11, 12, 13, it is observed that the field magnitude ΔE is of similar form and characteristics as for the field ΔE evaluated when $\Omega = 0.23\pi$ rad/sec, for the same angles (Figs. 7, 8, 9 and 10b respectively), with ΔE taking values of the same order of magnitude and with similar periodicity.

However, it is shown clearly that the range of Doppler shifts is greater for the increased angular rotational speed Ω studied here, for similar angles θ_i and φ_i. The Doppler spread increases linearly with the angular speed Ω, as shown by Eq. (12). Specifically, in Figs. 11(a), (b), when $\theta_i = 89°$, the Doppler shift range is $[-1215, 1215]$ Hz, while in Figs. 7, 8 for $\Omega = 0.23\pi$ rad/sec and the same θ_i, the
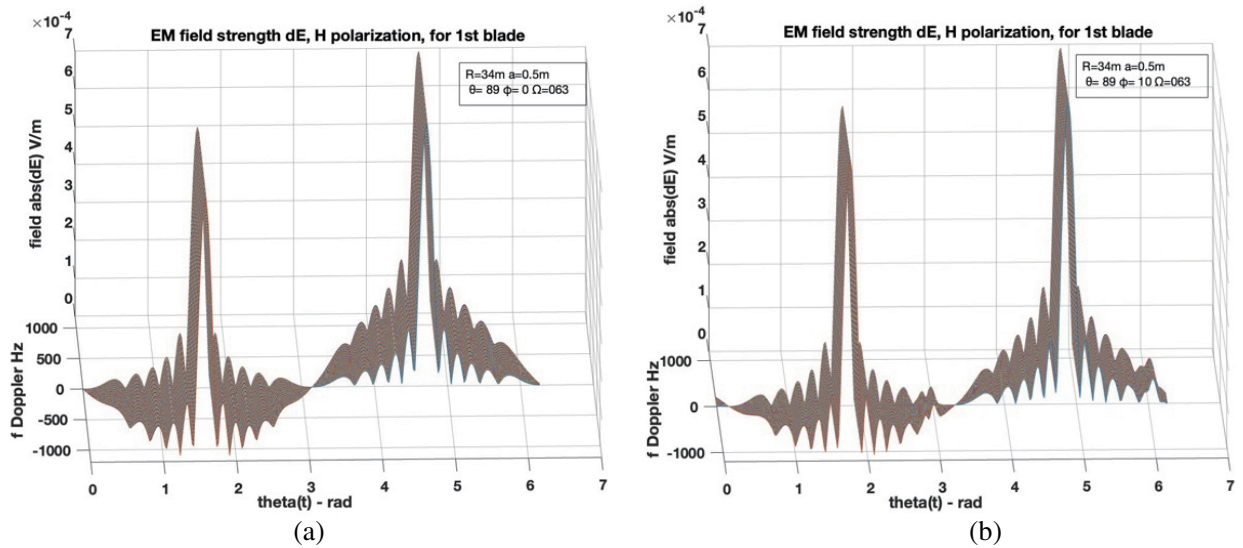

Figure 11. (a), (b) EM field ΔE $(f_d, \Theta(t))$ on one blade, $\Omega = 0.633\pi$ rad/sec, for $\theta_i = 89°$, $\varphi_i = 0$, $10°$.
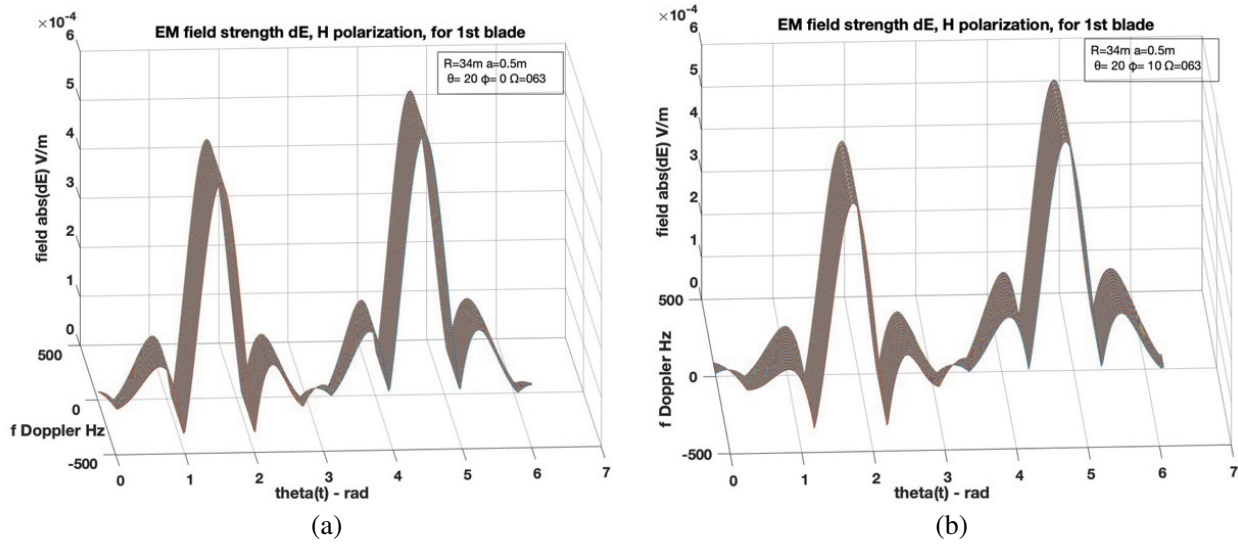
Figure 12. (a), (b) EM field ΔE (f_d, $\Theta(t)$) on one blade, $\Omega = 0.633\pi$ rad/sec, for $\theta_i = 20°$, $\varphi_i = 0, 10°$.
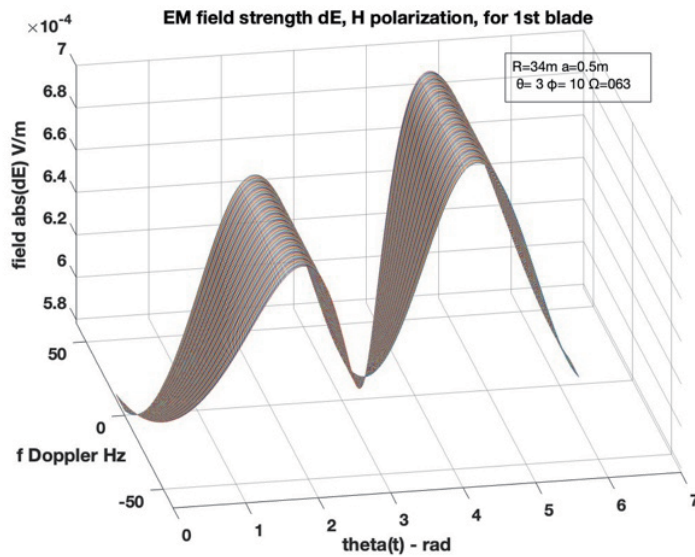

Figure 13. EM field ΔE (f_d, $\Theta(t)$) on one blade, $\Omega = 0.633\pi$ rad/sec, for $\theta_i = 3°$, $\varphi_i = 10°$.
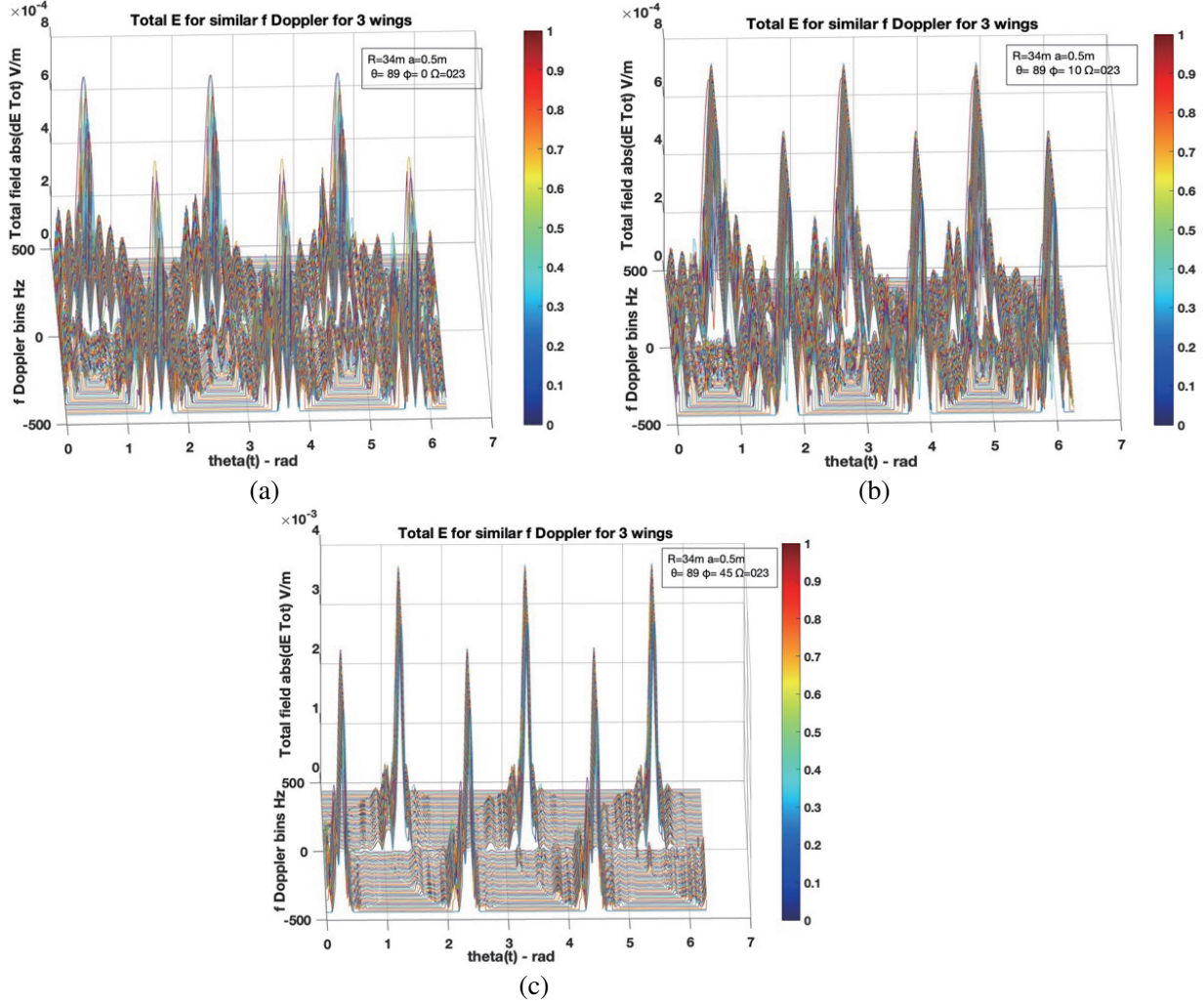
Doppler shift range is $[-442, 442]$ Hz. Similarly, for $\theta_i = 20°$ in Figs. 12(a), (b), the Doppler shift range is $[-415, 415]$ Hz, while in Fig. 9, for $\Omega = 0.23\pi$ rad/sec, it is $[-150, 150]$ Hz. For $\theta_i = 3°$ in Fig. 13, the Doppler shift range is $[-64, 64]$ Hz, whereas for $\Omega = 0.23\pi$ rad/sec, in Fig. 10(b), it is $[-23, 23]$ Hz. The Doppler spread can vary from 20 Hz to 1200 Hz depending on the blades' rotation conditions, as shown below in Table 1.

E) After the computation of the electric field magnitude $\Delta E(\Theta(t), \zeta)$ generated by each WT blade, the total electric field, E_{TOT}, is computed by a three-wing rotating WT illuminated by a radar. E_{TOT} will be received by the radar receiver as clutter, as described in Sections 1 and 2.

The total electric field E_{TOT} is evaluated, based on equation (20), as the vector sum of the fields $\Delta E(\Theta(t), \zeta)$ generated by sections (ζ, $\zeta + d\zeta$) of each blade that present the same Doppler frequency shift at the same moment in time. The Doppler shifts that occur during a full blade rotation take the same range of values for all three blades; however, it is observed that at a specific time t, on each

Table 1. Results of the Doppler shift range in case of a single blade.

Ω	0.23π rad/sec or 7 rpm						0.633π rad/sec or 19 rpm				
θ_i	89^0		20^0		0^0	3^0	89^0		20^0		3^0
φ_i	0^0	10^0	0^0	10^0	10^0	10^0	0^0	10^0	0^0	10^0	10^0
Δf_D Hz	±442		±150		-	±23	±1215		±415		±64

(a)

(b)

(c)

Figure 14. (a), (b), (c) Total Electric field E_{TOT} for $\theta_i = 89°$ and $\varphi_i = 0°$, $10°$, $45°$, $\Omega = 0.23\pi$ rad/s.

blade the Doppler shifts that are generated by the various strips $(\zeta, \zeta + d\zeta)$ of the blade take different values. This means that on each blade different points create the same Doppler shift at the same time t, depending on the instantaneous angle of the three blades. Thus, the various Doppler shifts occurring at the same moment in time by each blade are allocated to Doppler frequency bins of a small size. Then, the vector sum of the electric fields is calculated from the electric field vectors ΔE that belong to the same Doppler frequency bin at the same time t, on each blade. So, at time t, the total field strength, which is associated with the same Doppler shift f_d, is computed. This is based on the assumption that these electric fields, at the same time t, will have an additive (detrimental) effect on the signal detection by the radar, taking into account the different spatial phases of the EM wave. The Doppler frequency
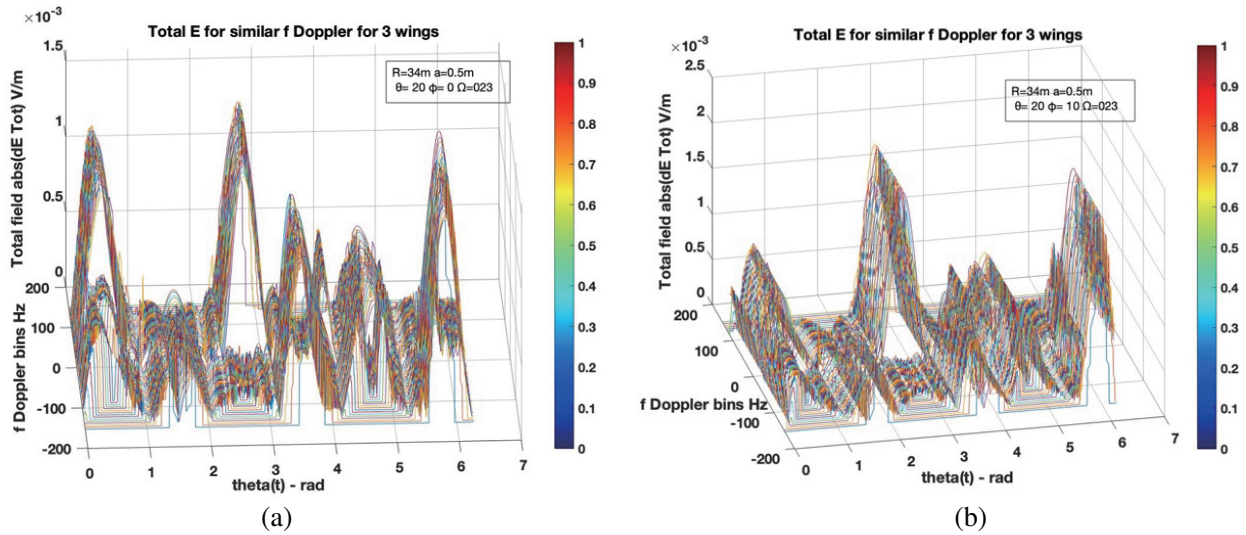
Figure 15. (a), (b) Total Electric field E_{TOT} for $\theta_i = 20°$ and $\varphi_i = 0°$, $10°$, $\Omega = 0.23\pi$ rad/s.
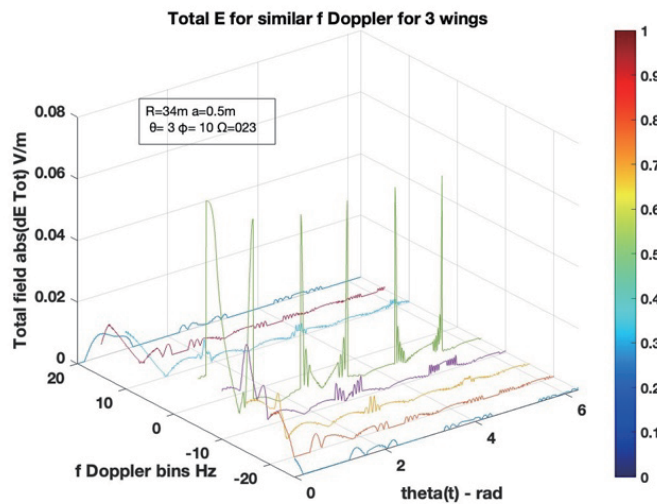

Figure 16. Total Electric field E_{TOT} for $\theta_i = 3°$ and $\varphi_i = 10°$, $\Omega = 0.23\pi$ rad/s.

bin size depends on the range of Doppler shifts in each case studied, and when about 100 bins are used the bin size ranges from 5 to 20 Hz.

The following graphs demonstrate the total electric field E_{TOT} evaluated for different cases of θ_i, φ_i and Ω, as studied in the previous sections.

It should be noted that the total electric field, around 0 Hz Doppler frequency, is omitted from the graphs (i.e., the bin containing the 0 Hz Doppler and the neighbouring one or two bins, depending on the bin range). This is because there are cases of $\Theta(t)$ where the electric field E_{TOT} is concentrated around 0 Hz Doppler only, creating an apparent surge of electric field, particularly for small angles θ_i. Moving Target Detection/Indicator Radars suppress the near zero Doppler frequencies.

Examining Figs. 14–17 it is observed that the total electric field magnitude E_{TOT} is symmetric, with a number of higher and lower magnitude peaks, which depend on angle θ_i. When θ_i is very small (3°) there are times ($\Theta(t)$) and Doppler frequencies, and when the total electric field magnitude E_{TOT} appears strong, mostly, at other times and frequencies f_d, the field strength E_{TOT} is attenuated. This is particularly evident in Figs. 16 and 17(c). In Fig. 17, for the increased angular rotation speed $\Omega = 0.633\pi$ rad/sec, the total electric field magnitude is of similar form, characteristics, and magnitude
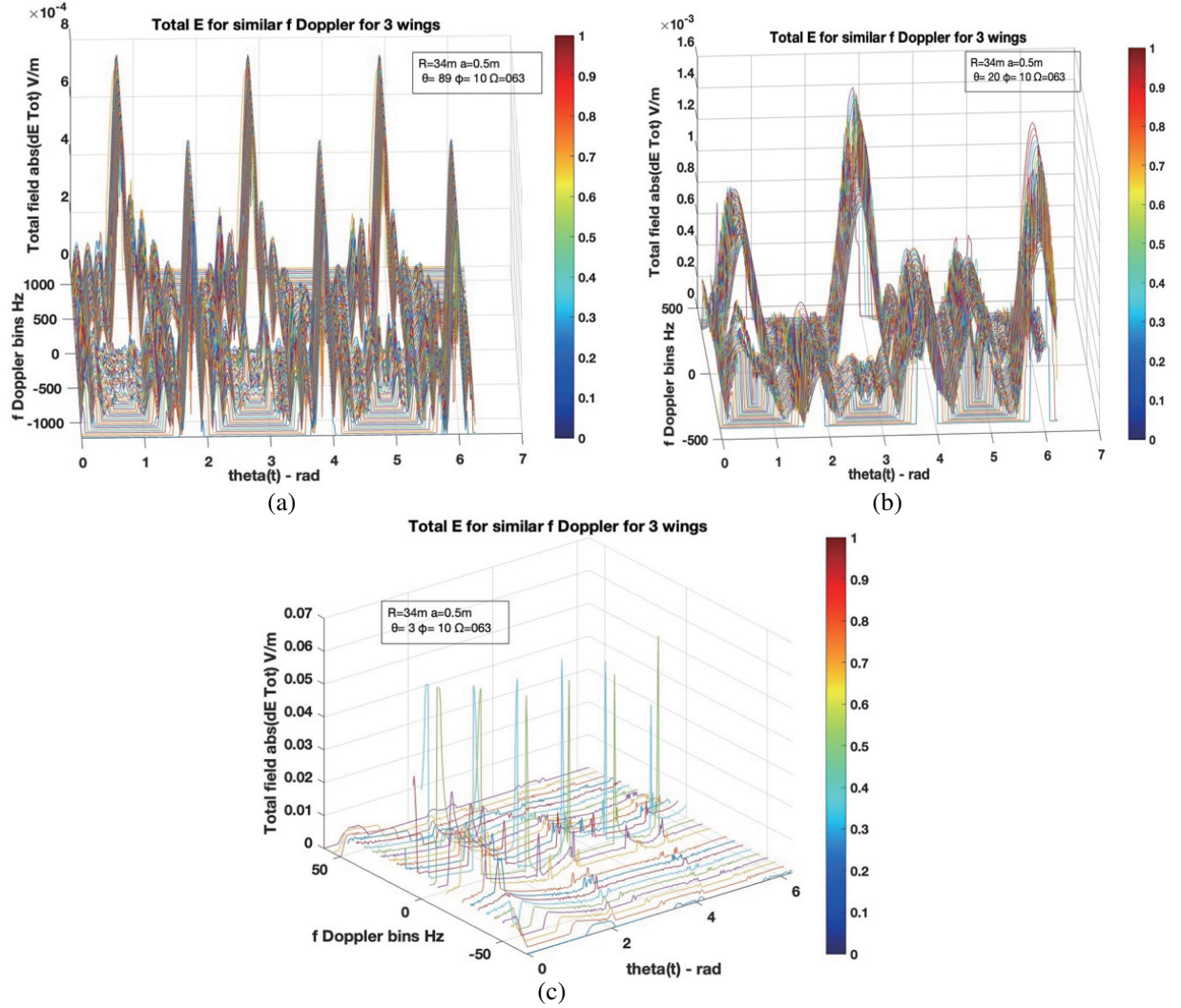
Figure 17. (a), (b), (c) Total Electric field E_{TOT} for $\theta_i = 89°$, $20°$, $3°$ and $\varphi_i = 10°$, $\Omega = 0.633\pi$ rad/s.

as that for the total electric field evaluated when $\Omega = 0.233\pi$ rad/sec, for the same angles (Figs. 14, 15, 16).

7. CONCLUSIONS

In this work a generalised method of computation of Electromagnetic wave scattering from rotating wind turbines is presented. To that end, the method of Physical Optics was implemented. Based on the approximative numerical theory developed, a simulation program was designed in MATLAB to evaluate the electric field strength and the Doppler frequency shifts generated from scattering on the blades of a wind turbine, and the results were presented. The reflections caused by the rotating WT blades generate complex Doppler patterns in coherent radars. The computed results show strong fluctuations with the change of WT rotation axis, as a result of wind direction and also relative elevation of the radar and WT rotation axis. It is observed that more than 30 dB signal fluctuations are present during a period of rotation of WT blades. Taking into account the high degree of complexity of spectral distribution it seems that a reasonable mitigation approach is in the time axis rather than a matched filter type approach. Placing time negation gates on the returning signals around the WT position seems to be the most effective method to mitigate the effect of backscattering from rotating blades. The results obtained are in agreement qualitatively with measurements presented in [4, 5].

Finally, it should be mentioned that the computational model presented could be useful for both radar developers and WT designers and manufactures (i.e., using microwave absorbers in the construction of blades), to use the simulation tool presented to mitigate or alleviate the undesired effects of WT echoes to Radars which use Doppler signal processing.

ACKNOWLEDGMENT

REFERENCES

1. Leonov, S., O. Hubbard, Z. Ding, H. Ghadaki, J. Wang, and T. Ponsford, "Advanced mitigating techniques to remove the effects of wind turbines and wind farms on primary surveillance radars," *IEEE 2008 Radar Conference*, Rome, doi:10.1109/RADAR.2008.4721114, Jun. 2008.

2. US Department of the Interior Bureau of Ocean Energy Management Office of Renewable Energy Programs, "Radar interference analysis for renewable energy facilities on the atlantic outer continental shelf," OCS Study BOEM 2020-039, Aug. 2020.

3. De La Vega, D., J. Matthews, L. Norin, and I. Angulo, "Mitigation techniques to reduce the impact of wind turbines on radar services," *MDPI, Energies (Special issue Wind Turbines)*, Vol. 6, No. 6, 2859–2873, doi: 10.3390/en6062859, Jun. 2013.

4. Wang, W.-Q., "Detecting and mitigating wind turbine clutter for airspace radar systems," *Hindawi, The Scientific World Journal*, Vol. 2013, No. Article ID 385182, 2013.

5. Bachmann, S., M. Lockheed, Y. Al-Rashid, P. Bronecke, R. Palmer, and B. Isom, "Suppression of the wind farm contribution from the atmospheric radar returns," *26th Conference on Interactive Information and Processing Systems (IIPS) for Meteorology, Oceanography, and Hydrology*, Jan. 2010.

6. Office of the Director of Defense Research and Engineering, "The effect of windmill farms on military readiness," 2006 Report to the Congressional Defense Committees, Washington DC, 20301, 2006.

7. Cuong, T., "Radar cross section (RCS) simulation for wind turbines," Naval Postgraduate School, Monterey, California, http://hdl.handle.net/10945/34754, 2013-06.

8. Shen, M., X. Wang, D. Wu, and D. Zhu, "Wind turbine clutter mitigation for weather radar by an improved low-rank matrix recovery method," *Progress In Electromagnetics Research M*, Vol. 88, 191–199, doi:10.2528/PIERM19103101, 2020.

9. Hegler, S. and D. Plettemeier, "Simulative investigation of the radar cross section of wind turbines," *MDPI, Applied Sciences*, Vol. 9, No. 19, 4024, Sep. 2019, doi: 10.3390/app9194024.

10. Lainer, M., J. Figueras, I Ventura, Z. Schauwecker, M. Gabella, M. F.-Bolaños, R. Pauli, and J. Grazioli, "Insights into wind turbine reflectivity and radar cross-section (RCS) and their variability using X-band weather radar observations," *Atmos. Meas. Tech. (AMT)*, Vol. 14, 3541–3560, https://doi.org/10.5194/amt-14-3541-2021, 2021.

11. Kent, B. M., K. C. Hil, A. Buterbaugh, G. Zelinski, R. Hawley, L. Cravens, Tri-Van, C. Vogel, and T. Coveyou, "Dynamic radar cross section and radar doppler measurements of commercial general electric windmill power turbines part 1: Predicted and measured radar signatures," *IEEE Antennas and Propagation Magazine*, Vol. 50, No. 2, 211–219, doi: 10.1109/MAP.2008.4562424, Apr. 2008.

12. Schubel, P. J. and R. J. Crossley, "Wind turbine blade design," *MDPI, Energies*, Vol. 5, No. 9, 3425–3449, doi:10.3390/en5093425, 2012.